Modelling the viral dynamics of the SARS-CoV-2 Delta and Omicron variants in different cell types

Clare P. McCormack[1]*, Ada W. C. Yan[2]*, Jonathan C. Brown[2], Ksenia Sukhova[2], Thomas P. Peacock[2], Wendy S. Barclay[2], Ilaria Dorigatti[1]

[1]MRC Centre for Global Infectious Disease Analysis, School of Public Health, Imperial College London, London, United Kingdom

[2]Department of Infectious Disease, Imperial College London, London, United Kingdom

*contributed equally, joint corresponding authors

Abstract

We use viral kinetic models fitted to viral load data from *in vitro* studies to explain why the SARS-CoV-2 Omicron variant replicates faster than the Delta variant in nasal cells, but slower than Delta in lung cells, which could explain Omicron's higher transmission potential and lower severity. We find that in both nasal and lung cells, viral infectivity is higher for Omicron but the virus production rate is higher for Delta. However, the differences are unequal between cell types, and ultimately leads to the basic reproduction number and growth rate being higher for Omicron in nasal cells, and higher for Delta in lung cells. In nasal cells, Omicron alone can enter via a TMPRSS2-independent pathway, but it is primarily increased efficiency of TMPRSS2-dependent entry which accounts for Omicron's increased activity. This work paves the way for using within-host mathematical models to understand the transmission potential and severity of future variants.

41 ## Introduction

42 Since its designation as a variant of concern (VOC) by the World Health Organization on 26th November
43 2021[1], the Omicron (B.1.1.529\BA.1) variant of severe acute respiratory coronavirus 2 (SARS-CoV-2)
44 has rapidly displaced the Delta (B.1.617.2) variant to become the dominant SARS-CoV-2 variant
45 globally[2–4]. Analyses have demonstrated that Omicron can partially evade the immunity generated
46 through previous infection and vaccination[5–8], thereby leading to reduced vaccine effectiveness
47 against symptomatic disease[9].

48 Despite this reduction in vaccine effectiveness against symptomatic disease, the risk of severe
49 outcomes (including hospital admission and death) following infection with Omicron is substantially
50 lower than following infection with Delta, for both vaccinated and unvaccinated individuals[10,11]. While
51 much remains to be understood about the mechanisms underpinning this observation, a reduction in
52 the capacity of Omicron relative to Delta to replicate in lung cells has been suggested as a possible
53 explanation[12]. On the other hand, Omicron's increased ability to replicate in nasal cells has been
54 suggested as an explanation for Omicron's transmission advantage over Delta observed from
55 epidemiological data[13–15].

56 It has been hypothesised that these differences in viral replication capacity in different cells can be
57 attributed to how Omicron and Delta utilise different pathways to enter host cells[12,16–18]. All SARS-CoV-
58 2 viruses can enter cells which express both ACE2 and TMPRSS2 proteins, via fusion of the viral and
59 cell membranes or via early endosomes[19]. However, Omicron is also able to efficiently enter ACE2+
60 cells via fusion from the endosome after endocytosis, without the involvement of TMPRSS2[16,20]. This
61 could expand the range of cells that Omicron can infect. A complication is by entering cells via the
62 endosome, SARS-CoV-2 may be inhibited by endosomal restriction factors such as interferon-induced
63 IFITM proteins[21,22] or NCOA7[23]. Understanding how virological properties shape the viral dynamics of
64 SARS-CoV-2 in different cell types can enhance our understanding of the mechanisms underlying the
65 observed differences in transmissibility between the Omicron and Delta variants. The different entry
66 pathways and their inhibition by endosomal restriction factors are shown in Figure 1.

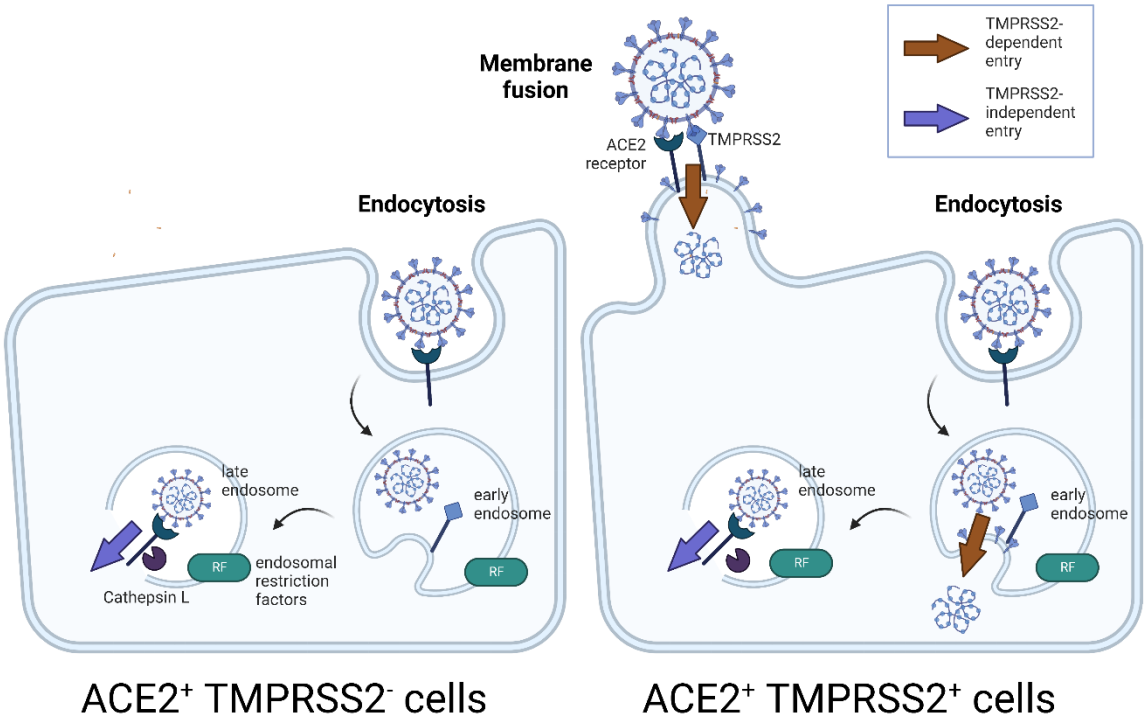

Figure 1. Illustration of TMPRSS2-dependent and TMPRSS2-independent entry pathways and their inhibition by endosomal restriction factors. In ACE2+ TMPRSS2+ cells (right), virus can enter in a TMPRSS2-dependent way via membrane fusion either at the cell surface or the early endosome; alternatively, virus can enter in a TMPRSS2-independent way through the late endosome. In ACE2+ TMPRSS2- cells (left), only the TMPRSS2-independent pathway is available. Both pathways can be inhibited by endosomal restriction factors. Created with BioRender.com.

Mechanistic mathematical models, calibrated against virological data, are a powerful tool for exploring viral dynamics as they provide a framework to quantify key characteristics of different variants and build an understanding of the drivers of inter-individual variation in response to infection. For example, previous within-host modelling studies of SARS-CoV-2 have enabled an understanding of the effect of covariates such as age, sex, and disease severity on viral load[24], the degree of heterogeneity between individuals[25], and the potential effect of antivirals and masking on viral load[26–30]. Models fitted to data from vaccine trials have suggested correlates of protection[31], while more theoretical immunological models have also been developed with the ultimate aim of understanding the interplay between the immune response and disease severity[32–34]. Studies linking the within- and between-host scales have improved the understanding of the relationship between Ct values and infectiousness[25,35], suggested characteristics of optimal testing regimes[36] and provided explanations for population-level epidemiological observations, e.g. the apparent reduction in viral load observed during the declining phase of an epidemic[37].

The studies mentioned above have all fitted their models to data from *in vivo* studies. While dynamics in humans are of ultimate interest, modelling viral kinetics and the immune response *in vivo* is

88 extremely complex. Moreover, studies in humans are often limited, with little or no information on
89 the timing and amount of the viral inoculum, sparse longitudinal observations, and often no available
90 measurements before the start of symptom onset[25,35]. *In vitro* studies offer a simplification of *in vivo*
91 dynamics, where both the inoculum and method of inoculation is controlled, and where some
92 components of the immune response – such as the adaptive immune response – are eliminated. Viral
93 load can be measured from the start of infection, which is important for estimating the growth rate
94 and basic reproduction number of the virus, which in turn can be used to assess the potential for load
95 variants to outcompete existing variants.

96 Here, using viral kinetics models calibrated against viral replication data generated through
97 experimental infection studies in primary human nasal epithelial cells (hNECs) and immortalised Calu-
98 3 lung cells, we characterise and compare the dynamics of Omicron and Delta viruses in each cell type
99 by quantifying key properties such as the basic reproduction number and growth rate, and by
100 exploring how these properties vary for different entry pathways, and in the presence and absence of
101 functional endosomal restriction factors.

102

103 # Methods

104 **Experimental Design/Data**

105 Full details of the viral kinetics experiments conducted are provided in Peacock et al.[20]. In brief, Calu-
106 3 and primary human nasal epithelial cells (hNECs) were inoculated with Omicron BA.1 and
107 Delta/B.1.617.2 isolates at an MOI of 0.001 (Calu-3) or 0.05 (hNECs), and incubated for 1 hr at 37°C.
108 The inoculum was then removed and, in the case of Calu-3 cells, replaced with 1 mL serum-free
109 DMEM. For Calu-3 cells, 100 µL of supernatant was collected for titration at 18, 24, 48 and 72 hours
110 post-infection. For hNECs, at the same timepoints post-infection, the supernatant was collected by
111 adding 200 µL of serum-free DMEM to the apical surface, incubating for 10 minutes, and removing for
112 collection.

113 Additional experiments were performed to investigate the effect of Camostat mesylate (henceforth
114 referred to as Camostat) and Amphotericin B on viral kinetics. Camostat is a serine protease inhibitor
115 and thus inhibits TMPRSS2, while Amphotericin B inhibits the restriction of viral endosomal entry by
116 endosomal restriction factors such as IFITM proteins[38–40]. Cells were pre-treated both basolaterally
117 and apically with either 50 µM of Camostat, 1µM of Amphotericin B or no drug for 2 hours prior to
118 infection, and this concentration of drug was maintained in the basolateral media throughout the
119 experiment. Infections and collection of timepoints were performed as above.

All experiments were performed in triplicate. Infectious viral titres were quantified by plaque assay and viral genome numbers were quantified by E gene RT-qPCR.

Mathematical Models

Model 1

To gain an initial understanding of the differences between the observed infection dynamics of the Omicron and Delta variants across each cell type, we first developed a simple model of the viral dynamics which assumed a single virus entry pathway for both variants. A simple schematic of the model is provided in Figure 2. Model equations are in the Supplementary Methods.

Target cells T become infected at a rate β (target cell infection rate) per infectious virion (V_{Inf}). The target cell infection rate is defined as the proportion of cells infected per day, per unit inoculum of 1 pfu/mL. Following an eclipse phase of mean duration of $1/\tau$ days, infectious cells (I) produce infectious and non-infectious virus. Infectious virus (V_{Inf}), as measured by plaque-assay, and total (infectious and non-infectious) virus (V_{RNA}), as measured by RT-qPCR, are produced at rates ω_{Inf} and ω_{RNA} respectively. (While the RT-qPCR assay could detect viral RNA released from lysed cells as well as from extracellular viral particles, the model assumes that all detected viral RNA originates from viral particles.) The duration of the eclipse phase $1/\tau$ reflects the speed of a single viral replication cycle, whereas the rate of viral production ω_{Inf} also reflects replication capacity. Infectious cells have a mean lifespan of $1/\delta$ days, and infectious and non-infectious virus is assumed to decay at rates κ_{Inf} and κ_{RNA} respectively, with additional loss due to entry into cells. Cells which express the ACE2 receptor, which is required for SARS-CoV-2 virus entry, are considered target cells.

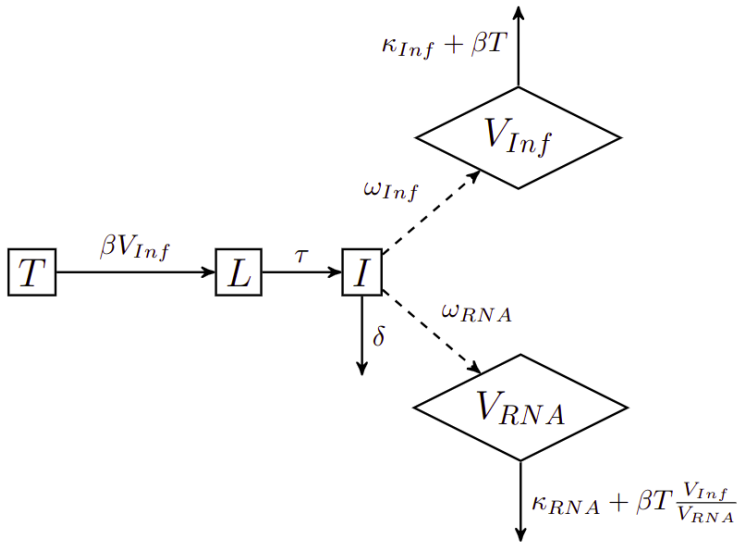

Figure 2: Compartmental diagram of model 1. Target cells T become infected at a rate β per infectious virion (V_{Inf}). Following an eclipse phase of mean duration of $1/\tau$ days, infectious cells (I) produce infectious virus as measured by plaque-assay (V_{Inf}) and total virus as measured by qPCR (V_{RNA}) at rates ω_{Inf} and ω_{RNA} respectively. Infected cells have a mean lifespan of $1/\delta$ days, and infectious and total virus are assumed to decay at rates κ_{Inf} and κ_{RNA} respectively.

Model 2

The experimental data showed that while Delta can only enter ACE2$^+$ cells by utilizing the TMPRSS2 protein, Omicron can enter these cells both through TMPRSS2- dependent and TMPRSS2-independent pathways. Thus, in Model 2 we modify Model 1 to account for the two possible cell entry pathways, where TMPRSS2-independent pathways can be used to infect all ACE2$^+$ cells, and TMPRSS2-dependent pathways can only infect ACE2$^+$ TMPRSS2$^+$ cells. We assume that all ACE2$^+$ cells become infected through TMPRSS2-independent pathways at a rate β_E per infectious virion (V_{Inf}) and that ACE2$^+$ TMPRSS2$^+$ target cells (T_+) also become infected through TMPRSS2-dependent pathways at a rate β_T per infectious virion. We assume that endosomal restriction factors decrease the infectivity through the TMPRSS2-independent pathways by a factor f_E, and through TMPRSS2-dependent pathways by a factor f_T. Cells infected through TMPRSS2-independent and TMPRSS2-dependent pathways (L_E and L_T respectively) undergo eclipse phases of mean duration $1/\tau_E$ and $1/\tau_T$ days respectively. Following the eclipse phase, infectious cells (I) behave as per Model 1. The flow diagram of Model 2 is described in Figure 3.

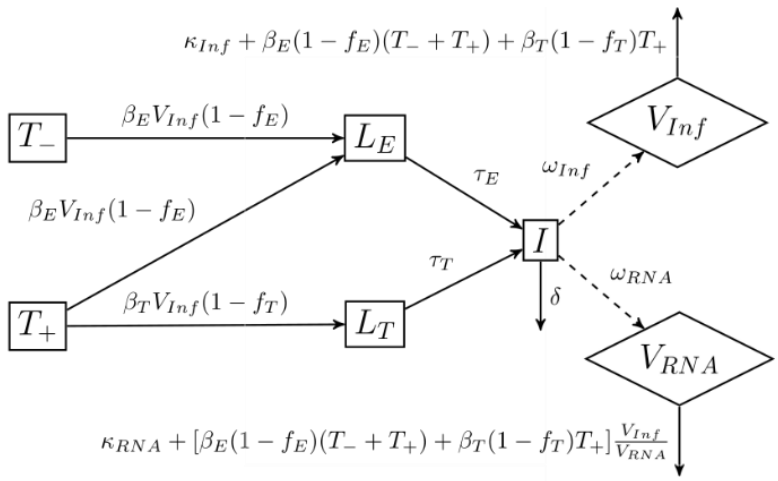

Figure 3: Compartmental diagram for Model 2. ACE2⁺ TMPRSS2⁻ target cells (T_-) become infected through TMPRSS2-independent pathways at a rate β_E per infectious virion (V_{Inf}). ACE2⁺ TMPRSS2⁺ target cells (T_+) become infected through TMPRSS2-independent pathways at a rate β_E per infectious virion, and through TMPRSS2 -dependent pathways at a rate β_T per infectious virion. Endosomal restriction factors decrease the infectivity through TMPRSS2-independent pathways by a factor f_E, and through TMPRSS2-dependent pathways by a factor f_T. Cells infected through TMPRSS2-independent and TMPRSS2-dependent pathways (L_E and L_T respectively) undergo eclipse phases of mean duration $1/\tau_E$ and $1/\tau_T$ days respectively. Following the eclipse phase, infectious cells (I) behave as per Model 1.

Model 2 is fitted to hNEC and Calu-3 data without drug, in the presence of Camostat, in the presence of Amphotericin B, and in the presence of both drugs. For each virus strain/cell type combination, all data (with and without drugs) is fitted simultaneously. Camostat is assumed to completely inhibit TMPRSS2-dependent pathways (we set $\beta_T = 0$); although Camostat also inhibits other serine proteases, but as TMPRSS2 is the main serine protease involved in SARS-CoV-2 virus entry, and because the activation of S2' in TMPRSS2-independent pathways likely occurs by cathepsin proteases rather than serine proteases, for simplicity we assume that Camostat does not affect TMPRSS2-independent pathways. Amphotericin B is assumed to completely remove endosomal restriction (we set $f_E = f_T = 0$).

Inferential framework

We calibrated the models to the observed data in a Bayesian inferential framework using Markov Chain Monte Carlo (MCMC) methods. In the results, we reported the median and 95% credible interval (CrI) of the parameter estimates. Full details of the model fitting algorithms are provided in the Supplementary Methods.

Results

<u>Data Description</u>

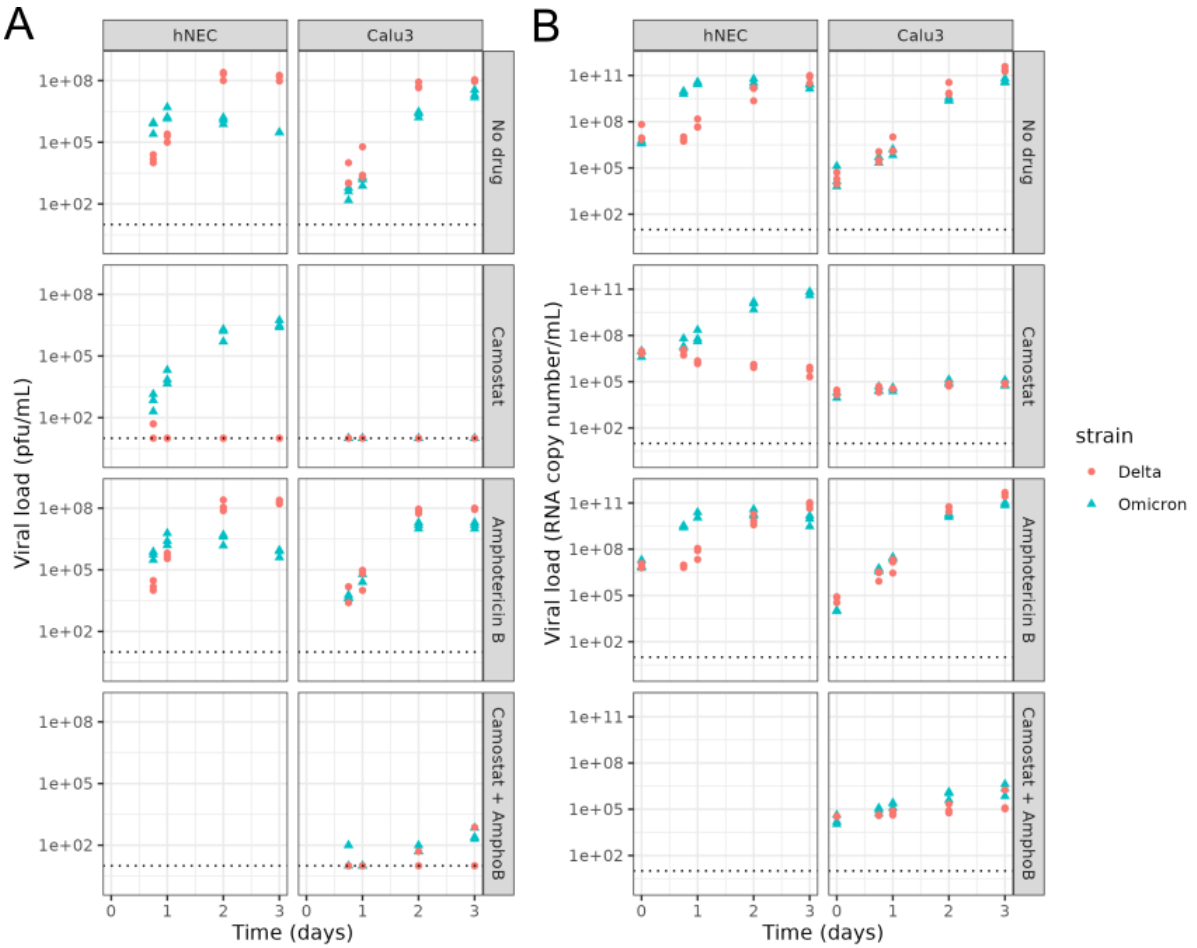

Figure 4: Summary of Data. (A) Infectious viral load (pfu/mL) quantified by plaque assay and (B) RNA copy number/mL quantified by RT-qPCR for Omicron (blue triangles) and Delta (red dots) for different cell types (columns) and drug treatments (rows). The dotted line shows the limit of detection; markers on the lines represent measurements below the limit of detection. Cells were infected on day 0.

Figure 4 summarises the study data. In control wells with no drug, temporal trends in viral growth varied both between strains and cell type. In hNECs, Omicron grew more rapidly than Delta, with viral load peaking by 1 day post infection (p.i.) for Omicron, compared with 2 days p.i. for Delta. However, despite this initial growth advantage, viral load was higher for Delta compared to Omicron at 3 days p.i.. In Calu-3 cells, the peak in viral load was observed 2-3 days p.i. for both Omicron and Delta. In contrast with hNECs where the strain corresponding to the highest viral load was dependent on measurement time, infectious and non-infectious viral load was higher for Delta than Omicron across all time points for Calu-3 cells.

In the presence of the drug Camostat which inhibits serine proteases, and thus TMPRSS2-dependent pathways, replication of Delta was severely inhibited in hNECs with no detectable increase in virus throughout the course of the experiment. In contrast, Omicron successfully replicated in hNECs in the presence of Camostat, albeit at a slower rate than in untreated wells. However, similar levels of viral

209 load were obtained by 2-3 days p.i. in both the presence and absence of Camostat. For both strains,
210 the presence of Amphotericin B had little impact on viral load dynamics in hNECs. In Calu-3 cells,
211 infectious virus was not detected at any point for either Omicron or Delta in the presence of Camostat.
212 In the presence of the drug Amphotericin B which is described as specifically inhibiting endosomal
213 restriction[22,39], Omicron infectious viral titres were consistently higher than in control wells, until 3
214 days p.i. when titres became similar. Delta geometric mean infectious viral titres were similar with
215 and without Amphotericin B.
216
217 Experiments with both drugs combined were only performed for Calu-3 cells. For both virus strains,
218 the infectious viral load was below the limit of detection in the presence of Camostat only. Adding
219 Amphotericin B raised the infectious viral load to above the limit of detection for all replicates for
220 Omicron, but only for some replicates for Delta (Figure 4).
221
222 **Viral Fitness**
223
224 **Model 1**

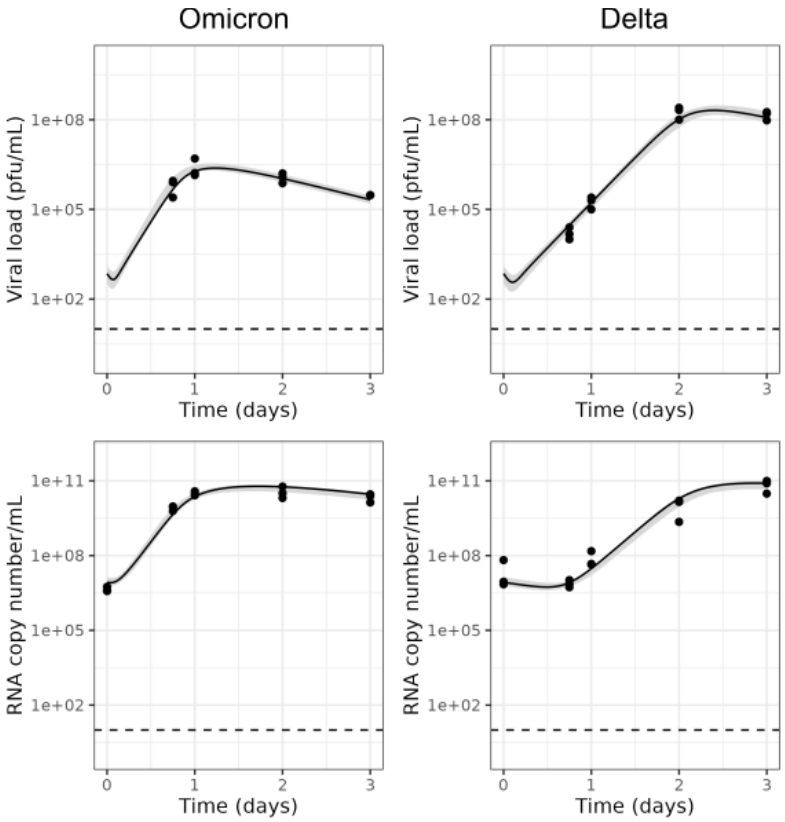

225

226 **Figure 5: Model 1 fits to data from hNECs without drugs.** Dots show the data, black lines show the maximum likelihood
227 fit, shaded areas show the 95% credible interval (CrI) and dotted lines show the limit of detection.

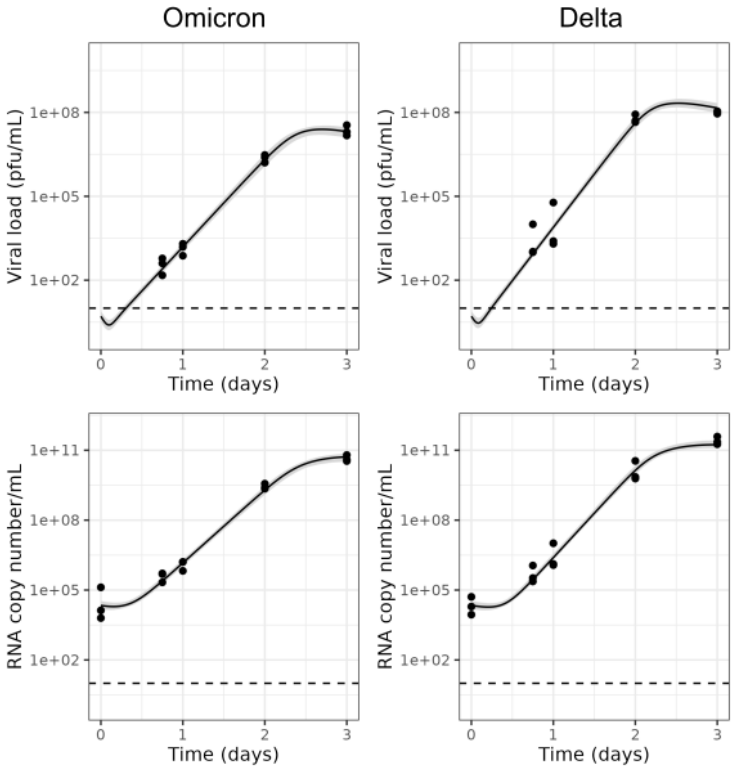

Figure 6: Model 1 fits to data from Calu-3 cells without drugs. Dots show the data, black lines show the maximum likelihood fit, shaded areas show the 95% credible interval (CrI) and dotted lines show the limit of detection.

For both Omicron and Delta, the simple model (Model 1) captured the viral dynamics observed in control wells of hNECs and Calu-3 cells (Figures 5, 6). For hNECs, we estimated a higher target cell infection rate β for Omicron relative to Delta (2.13e-05 (95% CrI: 1.54e-05, 3.07e-05) cell (pfu/mL)$^{-1}$ day^{-1} for Omicron, 8.89e-08 (95% CrI: 5.91e-08, 1.28e-07) cell (pfu/mL)$^{-1}$ day^{-1} for Delta), but a lower infectious virus production rate ω_{Inf} for Omicron relative to Delta (4.07e+03 (95% CrI: 3.13e+03, 5.50e+03) pfu/mL cell^{-1} day^{-1} for Omicron, 3.42e+05 (95% CrI: 2.41e+05, 5.04e+04) pfu/mL cell^{-1} day^{-1} for Delta). All estimated parameters are presented in Supplementary Table 2. These results suggest an approximately 1.5-fold difference in the growth rate between these strains in hNECs, with a growth rate of 11.61 day^{-1} (95% CrI: 10.43,12.99) for Omicron and 6.87 day^{-1} (95% CrI: 6.33,7.50) for Delta. Furthermore, we estimated a higher basic reproduction number (R_0) for Omicron (65.04 (95% CrI: 51.94, 82.71)) compared with Delta (23.13 (95% CrI: 19.91, 27.23)), thereby suggesting an overall increase in viral fitness of Omicron relative to Delta in hNECs.

For Calu-3 cells, we estimated a higher target cell infection rate for Omicron than Delta (9.23e-07 (95% CrI: 6.17e-07, 1.36e-06) cell (pfu/mL)$^{-1}$ day^{-1} for Omicron, 1.42e-07 (95% CrI: 9.80e-08, 2.05e-07) cell

247 (pfu/mL)$^{-1}$ day^{-1} for Delta) and lower infectious virus production rate for Omicron than Delta (4.13e+02
248 (95% CrI: 2.85e+02,6.07e+02) cell (pfu/mL)$^{-1}$ day^{-1} for Omicron, 3.73e+03 (95% CrI:
249 2.67e+03,5.32e+03) cell (pfu/mL)$^{-1}$ day^{-1} for Delta). In contrast with hNECs, our results indicate an
250 overall increase in viral fitness of Delta relative to Omicron in Calu-3 cells as we estimated a higher
251 basic reproduction number of Delta (36.67 (95% CrI: 33.69, 39.81)) compared to Omicron (24.23 (95%
252 CrI: 22.14, 26.70)) in this cell type. In addition, we estimated a larger growth rate of Delta relative to
253 Omicron in Calu-3 cells, with a growth rate of 8.78 day^{-1} (95% CrI: 8.40, 9.15) for Delta compared with
254 7.25 day^{-1} (95% CrI: 6.86, 7.60) for Omicron (for details see Supplementary Table 2).

255

256 For both cell types, the target cell infection rate (β), which is positively correlated with the probability
257 of a virion successfully infecting a cell, was higher for Omicron than Delta. The infectious virus
258 production rate (ω_{Inf}), which is directly proportional to the burst size (the total number of infectious
259 virions produced by one infected cell), was higher for Delta than Omicron. However, the magnitude
260 of each of these differences meant that the basic reproduction number and growth rate, which are
261 both functions of the target cell infection rate and the infectious virus production rate (see
262 Supplementary Methods), were higher for Omicron in hNECs, but higher for Delta in Calu-3 cells
263 (Supplementary Table 2).

264

265 **Model 2**

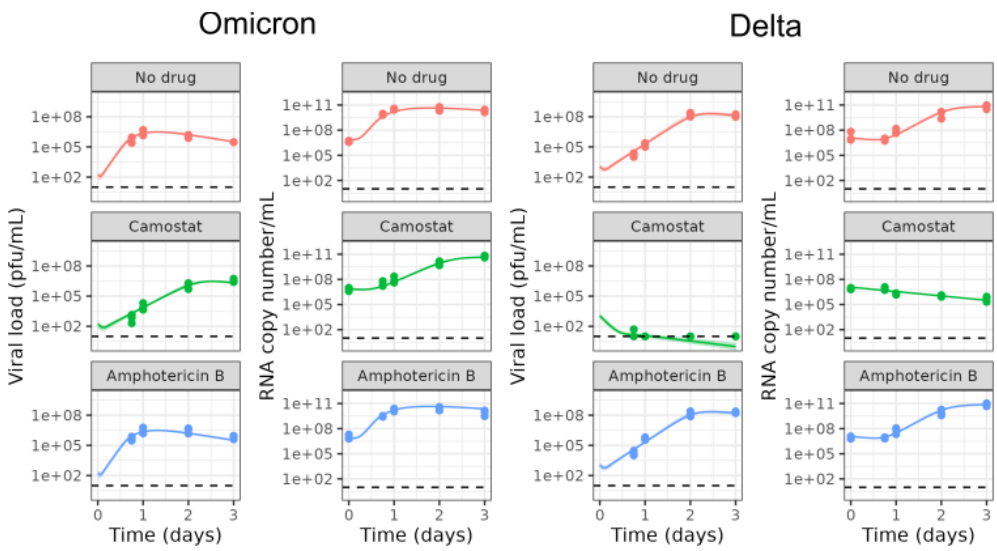

266

267 **Figure 7. Model 2 fits to data from hNECs with and without drugs.** Dots show the data, black lines show the maximum
268 likelihood fit, shaded areas show the 95% credible interval (CrI) and dotted lines show the limit of detection. Markers on
269 the lines represent measurements below the limit of detection.

270

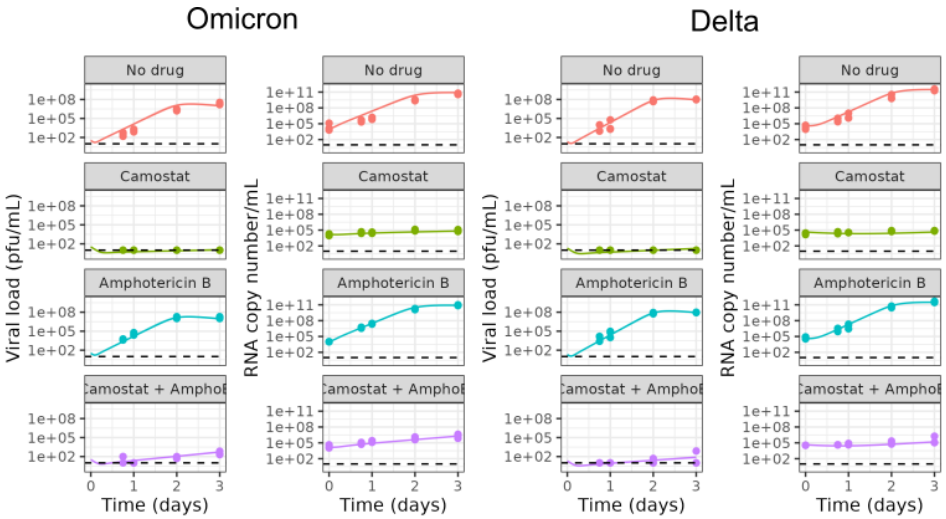

Figure 8. Model 2 fits to data from Calu-3 cells with and without drugs. Dots show the data, black lines show the maximum likelihood fit, shaded areas show the 95% credible interval (CrI) and dotted lines show the limit of detection. Markers on the lines represent measurements below the limit of detection.

When fitting Model 2 to the data, we found the same qualitative result that Omicron's R_0 is higher than Delta's in hNECs, but lower in Calu-3 cells (Figures 7 and 8). In hNECs, R_0 for Omicron was estimated to be 106.59 (95% CrI: 85.92, 134.72), while for Delta it was estimated to be 21.61 (95% CrI: 18.97, 25.30). In Calu-3 cells, R_0 for Omicron was estimated to be 16.53 (95% CrI: 15.15, 17.99), and for Delta was estimated to be 27.87 (95% CrI: 25.60, 30.34). R_0 estimates were comparable between Models 1 and 2, except for Omicron in hNECs, where the R_0 estimates obtained with Model 2 were higher. This discrepancy occurred because Model 2 predicts that Omicron can use both TMPRSS2-dependent and TMPRSS2-independent pathways in hNECs (see next section), whereas for all other strain and cell combinations only TMPRSS2-dependent pathways are active. When only TMPRSS2-dependent pathways are active, then in the absence of drug, Models 1 and Model 2 are the same. All parameter estimates are presented in Supplementary Table 1.

Role of Cell Entry Pathways

As Camostat inhibits serine proteases including TMPRSS2, Camostat-sensitive viruses must be able to use TMPRSS2-independent pathways for cell entry; thus, the fit of Model 2 to the data in the presence of Camostat provides information on the role of cell entry pathways. We found that in hNECs, Omicron was able to utilise both TMPRSS2-dependent and TMPRSS2-independent pathways. The median estimates of R_{0T} and R_{0E} were 92.13 (95% CrI: 72.95, 118.27) and 15.44 (95% CrI 12.86, 18.52) respectively (Supplementary Table 3). On the other hand, in hNECs, Delta was unable to effectively use TMPRSS2-independent pathways, as $R_{0E} < 1$ (median 0.15, 95% CrI: (0.07, 0.30)). In Calu-3s,

297 neither virus was able to use TMPRRS2-independent pathways effectively. R_{0E} was estimated to be
298 slightly greater than 1 for both Omicron (median 1.34 (95% CrI: 1.14, 1.55)) and Delta (median 1.71
299 (95% CrI: 1.47, 1.98)) but these small values of R_0 are insufficient for the viral load to exceed the limit
300 of detection during the time course of the experiment (Figure 8 Camostat panels). Note that for
301 Omicron in hNECs, the estimate for R_{0T} is comparable to the overall R_0 for Model 1. This is because
302 the increase in viral load due to TMPRSS2-dependent pathways is much faster than through TMPRSS2-
303 independent pathway, so the TMPRSS2-dependent pathway is the main contributor to the initial
304 exponential increase, from which Model 1 estimates R_0.
305
306 It has been suggested that Omicron's use of TMPRRS2-independent pathways explains its fitness
307 advantage over Delta[12,16,17]. However, even the TMPRSS2-specific basic reproduction number is higher
308 for Omicron than Delta in hNECs, with a median R_{0T} equal to 92.13 (95% CrI: 72.95, 118.27) for
309 Omicron compared to 21.46 (95% CrI:18.89, 25.05) for Delta. In fact, R_{0T} alone for Omicron is greater
310 than the overall R_0 for Delta. Therefore, it is primarily Omicron's more efficient use of TMPRSS2-
311 dependent pathways, rather than its utilisation of TMPRSS2-independent pathways, which gives it a
312 fitness advantage over Delta in hNECs.
313
314 **Role of endosomal restriction**
315
316 As Amphotericin B inhibits restrictions to virus entry imposed by endosomal restriction factors, the fit
317 of Model 2 to the Amphotericin B data provides information on the role of endosomal restriction
318 factors in shaping the viral dynamics observed. The parameters f_E and f_T capture the degree of
319 inhibition of TMPRSS2-independent and TMPRSS2-dependent pathways by endosomal restriction
320 factors respectively, and Amphotericin B is assumed to set these parameters to 0. Comparing across
321 cell types, inhibition by endosomal restriction factors was higher in Calu-3 cells than hNECs across all
322 strains and pathways (higher values of f_E and f_T for Calu-3 cells compared to hNEC cells in
323 Supplementary Table 4), with the exception of TMPRSS2-independent pathways for Delta, where f_E
324 could not be estimated precisely. Inhibition was similar for both Omicron and Delta in hNECs, but
325 Omicron was more inhibited by endosomal restriction factors than Delta in Calu-3 cells for both
326 pathways (higher values of f_E and f_T for Omicron than Delta in Calu-3 cells in Supplementary Table
327 4). Comparing across pathways, f_E and f_T were similar for each virus strain in hNECs, but in Calu-3
328 cells, f_E was higher than f_T for both virus strains, suggesting more inhibition of TMPRSS2-independent
329 pathways than of TMPRSS2-dependent pathways.
330

331 Given that TMPRSS2-independent pathways are susceptible to inhibition by endosomal restriction
332 factors, and that previous variants were not able to use endosomal restriction pathways, one may
333 hypothesise that Omicron has overcome endosomal restriction in hNECs, and that TMPRSS2-
334 independent pathways would also be accessible by other virus-cell combinations if endosomal
335 restriction were lifted. However, we predict that even if endosomal restriction is lifted for the three
336 other virus-cell combinations (as per the Amphotericin B experiments) R_{0EX} remains low. This
337 suggests that other factors contribute to Omicron's increased use of TMPRSS2-independent pathways
338 in hNECs. We predict that in the absence of endosomal restriction factors, Omicron would still have a
339 higher overall basic reproduction number and growth rate than Delta in hNECs, but these quantities
340 would be similar between variants in Calu-3 cells (R_{0X} in Supplementary Table 3 and r_X in
341 Supplementary Table 6).
342
343 **Changing the assumed eclipse phase duration**
344
345 A caveat of the above results is that we have fixed the length of the eclipse phase. The eclipse phase
346 in this model reflects the speed of viral replication with the cell. To date, studies which have measured
347 the duration of the eclipse phase in the SARS-CoV-2 viral life cycle have used viruses which enter target
348 cells through TMPRSS2-dependent pathways only[41,42]. Thus, the duration of the eclipse phase for
349 TMPRSS2-independent pathways is unclear and our knowledge of this component of the viral life cycle
350 is limited. To address this, we conducted a sensitivity analysis around the duration of the eclipse phase.
351 In Model 1, τ was set to 6, 4, or 2 day^{-1}. In Model 2, τ_T was set to 6, 4 or 2 day^{-1}, and τ_E was set to 4,
352 2 or 1 day^{-1}. We found that for Model 1, regardless of the duration of the eclipse phase assumed – as
353 long as it was the same between strains – Omicron had a higher R_0 than Delta in hNECs, and Delta
354 had a higher R_0 than Omicron in Calu-3 cells (Supplementary Table 4). Also, all estimated R_0 values
355 decreased as the duration of the eclipse phase decreased, as expected theoretically. This is because
356 if, at the start of infection, cells start producing virus sooner due to a short eclipse phase, then each
357 individual infected cell needs to lead to fewer secondary infections to reproduce the dynamics
358 observed. Similarly, for Model 2, we found that regardless of the values of τ_E and τ_T, as long as these
359 were assumed to be the same between strains, Omicron had a higher R_0 than Delta in hNECs, and
360 Delta had a higher R_0 than Omicron in Calu-3 cells; only Omicron in hNECs used TMPRSS2-independent
361 pathways efficiently; and endosomal restriction only had a significant effect in Calu-3 cells
362 (Supplementary Table 5). However, allowing the duration of the eclipse phase to be different between
363 strains, no longer allows us to draw conclusions about whether R_0 is greater for Omicron or Delta
364 (Supplementary Tables 3 and 5). On the other hand, estimates of the growth rate *r* only varied slightly

with the assumed duration of the eclipse phase for both models (Supplementary Tables 4 and 6).

Discussion

By fitting a simple within-host model to viral kinetics data for Omicron and Delta in hNECs and Calu-3 cells we found that Omicron has a fitness advantage over Delta in hNECs, but Delta has a fitness advantage over Omicron in Calu-3 cells, as measured by both the growth rate and basic reproduction number of the virus. These findings are consistent with previously published studies showing faster replication of Omicron compared with Delta in human nasal epithelial cells[14,16], and faster replication of Delta compared with Omicron in the ex vivo explant cultures of human lungs[12] and Calu-3 cells[43].

We estimated that Omicron had a higher rate of infection β in both cell types, which could be linked to increased ACE2 binding affinity, likely due to mutations in the spike protein. Evidence is mixed as to whether Omicron has a higher ACE2 binding affinity than Delta. Cameroni et al.[44] found that Omicron has a higher human ACE2 binding affinity than Delta, but Mannar et al.[45] found that ACE2 binding affinity is similar for Omicron and Delta, though higher than the ancestral strain. On the other hand, Zhang et al.[46] found that the Omicron spike protein required a higher level of ACE2 than Delta for efficient membrane fusion. We also estimated that Omicron had a lower rate of infectious virus production ω_{Inf} than Delta for both cell types. Changes to the rate of viral production could be due to mutations in either spike or non-spike proteins. The basic reproduction number is positively correlated with both the rate of infection β and the rate of infectious virus production ω_{Inf} in our models. In hNECs, the increase in the rate of infection β for Omicron was greater than the decrease in infectious virus production ω_{Inf}, resulting in a larger basic reproduction number and growth rate for Omicron compared to Delta; the converse was true in Calu-3 cells.

Previous studies have proposed that TMPRSS2-independent pathways which are only available to Omicron are responsible for its faster growth in hNECs. Our study found that Omicron can use TMPRSS2-independent pathways in hNECs, consistent with the previous studies. However, the growth rate and basic reproduction number for TMPRSS2-independent pathways was low and insufficient to explain the overall fitness advantage for Omicron over Delta in hNECs. On the other hand, the growth rate and basic reproduction number for TMPRSS2-dependent pathways was also higher for Omicron than Delta in hNECs and was sufficient to explain the overall fitness advantage. Evidence for the continued importance of TMPRSS2-dependent pathways for Omicron was provided by a study by Metzdorf et al.[47] which found that the growth of Omicron in the nose and lung was attenuated in TMPRSS2 knockout mice. In Calu-3 cells, neither Omicron nor Delta can use TMPRSS2-independent pathways, thereby providing further insight into how these viruses use different pathways to enter target cells.

400 We estimated the degree of inhibition in viral growth imposed by endosomal restriction factors by
401 fitting our model to data where the cells were treated with Amphotericin B, as Amphotericin B inhibits
402 the action of endosomal restriction factors. The main hypotheses tested were i) whether Omicron
403 was able to evade endosomal restriction in hNECs; ii) whether this evasion enabled Omicron to use
404 TMPRSS2-independent pathways; and iii) whether this was responsible for Omicron's growth
405 advantage. We found that the fitness of Delta in hNECs without endosomal restriction, as measured
406 by the basic reproduction number R_{0X} and the growth rate r_X, was still lower than that of Omicron in
407 hNECs with endosomal restriction. Hence, reduced endosomal restriction alone do not explain
408 Omicron's fitness advantage in hNECs. Although we were able to quantify the degree of inhibition by
409 endosomal restriction factors for both pathways for Omicron in hNECs, we were unable to do so for
410 Delta, as doing so requires either the infectious viral load to be above the limit of detection in the
411 presence of Camostat (as was the case for Omicron in hNECs), or requires data on viral growth in the
412 presence of both drugs (as was the case in Calu-3 cells). Hence, we were unable to make a direct
413 comparison at a pathway-specific level between Omicron and Delta in hNECs. In Calu-3 cells, we found
414 that Omicron was more inhibited by endosomal restriction factors than Delta, for either TMPRSS2-
415 dependent or TMPRSS2-independent pathways.

416 The model has several limitations. First, we fixed the infected cell death rate, the rate at which viruses
417 lose infectivity, the RNA degradation rate and the duration of eclipse phases, according to values from
418 the literature. It is currently unclear whether the duration of the eclipse phase differs between
419 variants. To test this, we conducted a sensitivity analysis where the model was fitted assuming
420 different lengths of the eclipse phase. This sensitivity analysis showed that if eclipse phase lengths
421 were assumed to be the same between Omicron and Delta, while the estimated values of R_0 changed
422 with the assumed length of the eclipse phase, the trends and relationships in R_0 and the growth rate
423 estimates r between Omicron and Delta (for example, that Omicron has a higher R_0 and growth rate
424 estimate r than Delta in hNECs) remained unchanged. Allowing the eclipse phase to be different
425 between strains, no longer allows us to draw conclusions about whether R_0 is greater for Omicron or
426 Delta (Supplementary Tables 3 and 5), but the differences in r are robust. This result reflects the
427 finding that if the eclipse phase is allowed to vary, the growth rate r is identifiable but R_0 is not. Future
428 studies could measure the duration of the eclipse phase for each cell type and virus strain using single-
429 cycle growth kinetics experiments.

430 We also did not test the effect of changing the assumed values of the infected cell or virus decay rates.
431 Studies have shown that Omicron survives for longer on surfaces than the ancestral strain[48] and
432 Delta[49], so it is plausible that extracellular virus may also differ in stability in our experiments.

433 Moreover, fixing the parameters using values from previous studies may underestimate the
434 uncertainty in $R_0$and r.

435 Another limitation of the model is that it assumes 100% effectiveness for both drugs. Assuming 100%
436 effectiveness of Camostat means interpreting all remaining viral growth as due to TMPRSS2-
437 independent pathways, so if the drug is less than 100% effective, the contribution of TMPRSS2-
438 independent pathways will be overestimated. Assuming 100% effectiveness of Amphotericin B means
439 interpreting viral growth in the presence of Amphotericin B as the viral growth in the complete
440 absence of endosomal restriction. If the drug were less than 100% effective, the viral load in the
441 complete absence of endosomal restriction could be higher than that suggested by the data, so the
442 effect of endosomal restriction would be underestimated.

443 Last, the structure of the model is such that the initial growth rate is independent of the inoculum
444 size. It is plausible that differences in growth rate between hNECs and Calu-3 cells observed in the
445 experiments were partly due to the differing inoculum sizes used, as a higher inoculum could, for
446 example, trigger endosomal restriction factors more quickly – an effect which was not modelled. A
447 higher multiplicity of infection (MOI) was used for hNECs as a lower MOI did not always successfully
448 infect these primary cells; repeating the Calu-3 experiments at the same higher MOI would strengthen
449 confidence in our comparison between cell types.

450 The models developed in this study can inform future studies using more complex models. Models
451 capturing more immune components and how the virus spreads within the host are useful for
452 understanding contributors to disease severity and the effects of antivirals[32–34], but because they have
453 many parameters, it is often difficult to determine their values by fitting them to data. This study can
454 help parameterize these models.

455 The models developed in this study can be applied to different SARS-CoV-2 virus strains to help
456 enhance our understanding of transmission potential of new strains as the virus continues to evolve.
457 While between-strain differences in the speed of viral replication is typically assessed by comparing
458 viral titre measurements at individual timepoints, adopting a mathematical modelling approach using
459 longitudinal timepoints enables us to estimate key characteristics of different strains such as the
460 growth rate and viral fitness, thus providing a deeper insight into the factors shaping observed
461 differences in viral dynamics at the individual and population level.

462

463 ## References

464 1. WHO. Classification of Omicron (B.1.1.529): SARS-CoV-2 Variant of Concern. *Who* 1
465 https://www.who.int/news/item/26-11-2021-classification-of-omicron-(b.1.1.529)-sars-cov-
466 2-variant-of-concern (2021).

467 2. GISAID. GISAID - hCov19 Variants. *Gisaid* https://gisaid.org/hcov19-variants/ (2022).

468 3. WHO. Tracking SARS-CoV-2 variants. *Who* https://www.who.int/en/activities/tracking-SARS-
469 Co Preprint at (2021).

470 4. Viana, R. *et al.* Rapid epidemic expansion of the SARS-CoV-2 Omicron variant in southern
471 Africa. *Nature* **603**, 679–686 (2022).

472 5. Cele, S. *et al.* Omicron extensively but incompletely escapes Pfizer BNT162b2 neutralization.
473 *Nature* **602**, 654–656 (2022).

474 6. Planas, D. *et al.* Considerable escape of SARS-CoV-2 Omicron to antibody neutralization.
475 *Nature* **602**, 671–675 (2022).

476 7. Cao, Y. *et al.* Omicron escapes the majority of existing SARS-CoV-2 neutralizing antibodies.
477 *Nature* **602**, 657–663 (2022).

478 8. Dejnirattisai, W. *et al.* SARS-CoV-2 Omicron-B.1.1.529 leads to widespread escape from
479 neutralizing antibody responses. *Cell* **185**, 467-484.e15 (2022).

480 9. Andrews, N. *et al.* Covid-19 Vaccine Effectiveness against the Omicron (B.1.1.529) Variant.
481 *New England Journal of Medicine* **386**, 1532–1546 (2022).

482 10. Nyberg, T. *et al.* Comparative analysis of the risks of hospitalisation and death associated with
483 SARS-CoV-2 omicron (B.1.1.529) and delta (B.1.617.2) variants in England: a cohort study. *The*
484 *Lancet* **399**, 1303–1312 (2022).

485 11. Wolter, N. *et al.* Early assessment of the clinical severity of the SARS-CoV-2 omicron variant in
486 South Africa: a data linkage study. *The Lancet* **399**, 437–446 (2022).

487 12. Hui, K. P. Y. Y. *et al.* SARS-CoV-2 Omicron variant replication in human bronchus and lung ex
488 vivo. **603**, (2022).

489 13. Willett, B. J. *et al.* SARS-CoV-2 Omicron is an immune escape variant with an altered cell entry
490 pathway. *Nature Microbiology 2022 7:8* **7**, 1161–1179 (2022).

491 14. Barut, G. T. *et al.* The spike gene is a major determinant for the SARS-CoV-2 Omicron-BA.1
492 phenotype. *Nat Commun* **13**, 1–14 (2022).

493 15. Lyngse, F. P. *et al.* Household transmission of the SARS-CoV-2 Omicron variant in Denmark.
494 *Nat Commun* **13**, 5573 (2022).

495 16. Willett, B. J. *et al.* SARS-CoV-2 Omicron is an immune escape variant with an altered cell entry
496 pathway. *Nat Microbiol* (2022) doi:10.1038/s41564-022-01143-7.

497 17. Meng, B. *et al.* Altered TMPRSS2 usage by SARS-CoV-2 Omicron impacts infectivity and
498 fusogenicity. *Nature 2022 603:7902* **603**, 706–714 (2022).

499 18. Suzuki, R. *et al.* Attenuated fusogenicity and pathogenicity of SARS-CoV-2 Omicron variant.
500 *Nature* **603**, 700–705 (2022).

501 19. Hoffmann, M. *et al.* SARS-CoV-2 Cell Entry Depends on ACE2 and TMPRSS2 and Is Blocked by
502 a Clinically Proven Protease Inhibitor. *Cell* **181**, 271-280.e8 (2020).

503 20. Peacock, T. P. *et al.* The altered entry pathway and antigenic distance of the SARS-CoV-2
504 Omicron variant map to separate domains of spike protein. *bioRxiv* 2021.12.31.474653 (2022)
505 doi:10.1101/2021.12.31.474653.

506 21. Winstone, H. *et al.* The Polybasic Cleavage Site in SARS-CoV-2 Spike Modulates Viral
507 Sensitivity to Type I Interferon and IFITM2. *J Virol* **95**, e02422-20 (2021).

508 22. Peacock, T. P. *et al.* The furin cleavage site in the SARS-CoV-2 spike protein is required for
509 transmission in ferrets. *Nat Microbiol* **6**, 899–909 (2021).

510 23. Khan, H. *et al.* TMPRSS2 promotes SARS-CoV-2 evasion from NCOA7-mediated restriction.
511 *PLoS Pathog* **17**, e1009820 (2021).

512 24. Challenger, J. D. *et al.* Modelling upper respiratory viral load dynamics of SARS-CoV-2. *BMC*
513 *Med* **20**, 25 (2022).

514 25. Ke, R., Zitzmann, C., Ho, D. D., Ribeiro, R. M. & Perelson, A. S. In vivo kinetics of SARS-CoV-2
515 infection and its relationship with a person's infectiousness. *Proc Natl Acad Sci U S A* **118**,
516 e2111477118 (2021).

517 26. Gonçalves, A. *et al.* Timing of Antiviral Treatment Initiation is Critical to Reduce SARS-CoV-2
518 Viral Load. *CPT Pharmacometrics Syst Pharmacol* **9**, 509–514 (2020).

519 27. Gonçalves, A. *et al.* SARS-CoV-2 viral dynamics in non-human primates. *PLoS Comput Biol* **17**,
520 (2021).

521 28. Perelson, A. S. & Ke, R. Mechanistic Modeling of SARS-CoV-2 and Other Infectious Diseases
522 and the Effects of Therapeutics. *Clin Pharmacol Ther* **109**, 829–840 (2021).

523 29. Koelle, K. *et al.* Masks Do No More Than Prevent Transmission: Theory and Data Undermine
524 the Variolation Hypothesis. Preprint at https://doi.org/10.1101/2022.06.28.22277028 (2022).

525 30. Ito, K., Piantham, C. & Nishiura, H. Relative instantaneous reproduction number of Omicron
526 SARS-CoV-2 variant with respect to the Delta variant in Denmark. *J Med Virol* **94**, 2265–2268
527 (2022).

528 31. Alexandre, M. *et al.* Modelling the response to vaccine in non-human primates to define
529 SARS-CoV-2 mechanistic correlates of protection. *Elife* **11**, e75427 (2022).

530 32. Jenner, A. L. *et al.* COVID-19 virtual patient cohort suggests immune mechanisms driving
531 disease outcomes. *PLoS Pathog* **17**, e1009753 (2021).

532 33. Rowlatt, C. F. *et al.* Modelling the within-host spread of SARS-CoV-2 infection, and the
533 subsequent immune response, using a hybrid, multiscale, individual-based model. Part I:
534 Macrophages. *bioRxiv* (2022) doi:10.1101/2022.05.06.490883.

535 34. Getz, M. *et al.* Iterative community-driven development of a SARS-CoV-2 tissue simulator.
536 *bioRxiv* (2021) doi:10.1101/2020.04.02.019075.

537 35. Marc, A. *et al.* Quantifying the relationship between SARS-CoV-2 viral load and infectiousness.
538 *Elife* **10**, e69302 (2021).

539 36. Larremore, D. B. *et al.* Test sensitivity is secondary to frequency and turnaround time for
540 COVID-19 screening. *Sci Adv* **7**, eabd5393 (2021).

541 37. Hay, J. A. *et al.* Estimating epidemiologic dynamics from cross-sectional viral load
542 distributions. *Science (1979)* **373**, eabh0635 (2021).

543 38. Brass, A. L. *et al.* The IFITM Proteins Mediate Cellular Resistance to Influenza A H1N1 Virus,
544 West Nile Virus, and Dengue Virus. *Cell* **139**, 1243–1254 (2009).

545 39. Lin, T.-Y. *et al.* Amphotericin B Increases Influenza A Virus Infection by Preventing IFITM3-
546 Mediated Restriction. *Cell Rep* **5**, 895–908 (2013).

547 40. Qian, J. *et al.* Primate lentiviruses are differentially inhibited by interferon-induced
548 transmembrane proteins. *Virology* **474**, 10–18 (2015).

549 41. Brahim Belhaouari, D. *et al.* The Strengths of Scanning Electron Microscopy in Deciphering
550 SARS-CoV-2 Infectious Cycle. *Front Microbiol* **11**, 2014 (2020).

551 42. Hou, Y. J. *et al.* SARS-CoV-2 D614G variant exhibits efficient replication ex vivo and
552 transmission in vivo. *Science (1979)* **370**, 1464–1468 (2020).

553 43. Shuai, H. *et al.* Attenuated replication and pathogenicity of SARS-CoV-2 B.1.1.529 Omicron.
554 *Nature* **603**, 693–699 (2022).

555 44. Cameroni, E. *et al.* Broadly neutralizing antibodies overcome SARS-CoV-2 Omicron antigenic
556 shift. *Nature* **602**, 664–670 (2022).

557 45. Mannar, D. *et al.* SARS-CoV-2 Omicron variant: Antibody evasion and cryo-EM structure of
558 spike protein–ACE2 complex. *Science (1979)* **375**, 760–764 (2022).

559 46. Zhang, J. *et al.* Structural and functional impact by SARS-CoV-2 Omicron spike mutations. *Cell*
560 *Rep* **39**, 110729 (2022).

561 47. Metzdorf, K. *et al.* TMPRSS2 Is Essential for SARS-CoV-2 Beta and Omicron Infection. *Viruses*
562 **15**, 271 (2023).

563 48. Chin, A. W. H., Lai, A. M. Y., Peiris, M. & Man Poon, L. L. Increased Stability of SARS-CoV-2
564 Omicron Variant over Ancestral Strain. *Emerging Infectious Disease journal* **28**, 1515 (2022).

565 49. Hirose, R. *et al.* Differences in environmental stability among SARS-CoV-2 variants of concern:
566 Both Omicron BA.1 and BA.2 have higher stability. *Clinical Microbiology and Infection* (2022)
567 doi:https://doi.org/10.1016/j.cmi.2022.05.020.

568

569 # Acknowledgements

570 CMC and ID acknowledge funding from the MRC Centre for Global Infectious Disease Analysis
571 (reference MR/R015600/1), jointly funded by the UK Medical Research Council (MRC) and the UK
572 Foreign, Commonwealth & Development Office (FCDO), under the MRC/FCDO Concordat agreement
573 and is also part of the EDCTP2 programme supported by the European Union. AWCY acknowledges
574 funding from an Imperial College Research Fellowship. ID acknowledges funding by the Wellcome

Trust and Royal Society (grant number 213494/Z/18/Z). This study was conducted as part of G2P-UK National Virology consortium funded by MRC/UKRI (MR/W005611/1). For the purpose of open access, the authors have applied a CC BY public copyright licence to any Author Accepted Manuscript version arising from this submission.

Author Contributions

CMC, AWCY, WSB and ID conceived the study; JCB and KS generated the *in-vitro* data; CMC, AWCY and ID conceived the mathematical models; CMC performed the analysis for Model 1; AWCY performed the analysis for Model 2; CMC, AWCY, JCB, TPP, WSB, and ID contributed to the interpretation of the results; CMC and AWCY wrote the first draft of the manuscript; all authors reviewed and approved the final version of the manuscript.

Competing Interests

The authors declare no competing financial interests.